Journal of Biomedical Optics

BiomedicalOptics.SPIEDigitalLibrary.org

Estimation of cerebral metabolic rate of oxygen consumption using combined multiwavelength photoacoustic microscopy and Doppler microultrasound

Yan Jiang
Roger Zemp

SPIE.

Yan Jiang, Roger Zemp, "Estimation of cerebral metabolic rate of oxygen consumption using combined multiwavelength photoacoustic microscopy and Doppler microultrasound," *J. Biomed. Opt.* **23**(1), 016009 (2018), doi: 10.1117/1.JBO.23.1.016009.

Journal of Biomedical Optics 23(1), 016009 (January 2018)

Estimation of cerebral metabolic rate of oxygen consumption using combined multiwavelength photoacoustic microscopy and Doppler microultrasound

Yan Jiang and Roger Zemp*
University of Alberta, Department of Electrical and Computer Engineering, Alberta, Edmonton, Canada

Abstract. The metabolic rate of oxygen consumption is an important metric of tissue oxygen metabolism and is especially critical in the brain, yet few methods are available for measuring it. We use a custom combined photoacoustic-microultrasound system and demonstrate cerebral oxygen consumption estimation *in vivo*. In particular, the cerebral metabolic rate of oxygen consumption was estimated in a murine model during variation of inhaled oxygen from hypoxia to hyperoxia. The hypothesis of brain autoregulation was confirmed with our method even though oxygen saturation and flow in vessels changed. [DOI: 10.1117/1.JBO.23.1.016009]

Keywords: photoacoustic imaging; oxygen metabolism; blood flow imaging; functional imaging; brain autoregulation.

Paper 170381RR received Jun. 13, 2017; accepted for publication Nov. 16, 2017; published online Jan. 18, 2018.

1 Introduction

The brain is one of the most energy-demanding and metabolically active organs of the body. Although it comprises only 2% of body weight, it receives about 15% of cardiac output and uses 20% of total body oxygen and 25% of total body glucose.[1] Under normal physiological conditions, oxidative metabolism of glucose is the primary way to produce adenosine triphosphate, the most important energy source for the brain. Oxygen needs to be delivered to the cerebral tissue at a rate that is biochemically appropriate to neurons' metabolic needs.[1] The cerebral metabolic rate of oxygen ($CMRO_2$) depends on the density of neurons and on their state of functional activation.[2] Many of the common disorders of the brain, such as Alzheimer's, Parkinson's, Huntington's, and others, have been found to be associated with alterations in the cerebral oxygen metabolism.[3–5] Therefore, the measure of $CMRO_2$ would not only enable a better understanding of the normal physiology during rest, sleep, anesthesia, aging, or functional brain tasks[6,7] but also be important for research and clinical applications related to brain disorders, stroke, and help to improve the management of patients who are at the risk of developing brain hypoxia-ischemia.[8,9]

Since the extraction of oxygen from cerebral tissue is closely matched to the brain's metabolic needs, $CMRO_2$ should be equal to the total amount of oxygen delivered to the cerebral tissue per unit time minus the amount leaving in the venous circulation per unit time.[2] As shown in Eq. (1), the cerebral blood flow (CBF) and the arteriovenous oxygen difference ($AVDO_2$) are the key parameters to estimate $CMRO_2$ based on Fick's principle.[10] Under steady-state physiologic conditions, $CMRO_2$ remains relatively constant over a range of arterial partial pressure of oxygen (PaO_2), typically 23 to 100 mm Hg, due to the cerebral autoregulation mechanism.[2] During mild hypoxia ($PaO_2 < 90$ mm Hg), the oxygen supply may be inadequate; however, metabolic demand may still be met by elevated CBF or reduced venous blood saturation, which means the higher extraction of oxygen from the blood.[11] Severe hypoxia ($PaO_2 <$ 30 mm Hg) may cause significant decrease in $CMRO_2$ due to insufficient blood flow or oxygen extraction compensation.[12] The metabolic autoregulation is a negative feedback system that seeks to balance the oxygen supply to its demand in a certain range[13]

$$CMRO_2 = CBF \times AVDO_2. \tag{1}$$

Currently, techniques to obtain $CMRO_2$ are limited. The important criteria for such techniques include noninvasiveness, adequate spatial and temporal resolution, low-radiation exposure, good safety profile, and widespread clinical availability.[14] Unfortunately, no *in vivo* method can fulfill all of these requirements. In early studies, the jugular vein oximetry involving catheterization has been used for a surrogate measure of $CMRO_2$ but is invasive.[15] Positron emission tomography (PET) with ^{15}O-labled radiotracers provides the most direct measurement of $CMRO_2$.[16] Yet, the spatial resolution is poor (~1 cm for clinical system), and the high ionizing radiation dose prevents its repeated use on the same patient. Magnetic resonance imaging (MRI) is also applied to image $CMRO_2$ by utilizing the blood oxygenation-level-dependent (BOLD) effect. BOLD MRI is noninvasive and can be performed with high spatial resolution, but it is only sensitive to deoxy-hemoglobin and has trouble distinguishing between changes in oxygen saturation and blood flow.[17] In recent studies, phase-contrast MRI has been proposed to quantify the blood flow in major inflow vessels; however, for the oxygen saturation estimation, only a large-sized vein (superior sagittal sinus) can be targeted.[18] Moreover, the complex

---

*Address all correspondence to: Roger Zemp, E-mail: rzemp@ualberta.ca

setup and high expenses preclude PET and MRI for many bedside clinical applications.

Imaging techniques based on optical contrast, which are sensitive to blood functional parameters, have been widely employed for the assessment of tissue oxygen metabolism. Near-infrared spectroscopy offers a means to estimate $CMRO_2$ noninvasively with the blood flow information provided by diffuse correlation spectroscopy.[19,20] The main drawback is that the spatial resolution is relatively low due to strong optical scattering. Photoacoustic imaging overcomes this limitation by ultrasonically imaging optical contrast through the photoacoustic effect.[21] Optical-resolution photoacoustic microscopy (OR-PAM) has been used to estimate oxygen consumption in superficial tissues.[22] This technique utilizes fine optical focusing to achieve high lateral resolution ($\sim 5\ \mu m$); however, the imaging depth is shallow (<1 mm) and the detectable flow speed (<12 mm/s) is limited due to low laser repetition rate.[23] While recent work suggests hope for photoacoustic flow estimation in deep tissues (>1 mm) using acoustic-resolution photoacoustic imaging,[24] it is less established than Doppler ultrasound methods we selected in this paper.

Here, we propose $CMRO_2$ estimation using photoacoustic and Doppler ultrasound methods. The combination of local blood oxygenation estimation and flow estimation in deep vessels is accomplished with a custom photoacoustic and microultrasound scanning system. We previously demonstrated oxygen flux estimation in a phantom study using such a system.[25] In this paper, the $CMRO_2$ is estimated *in vivo* by combining the measurements of arterial and venous oxygen saturation and flow rate of the internal jugular vein.

2 Materials and Methods

2.1 *Experiment Setup*

Our custom photoacoustic and microultrasound system was constructed by a combined light delivery and ultrasound probe, a tunable laser, a computer-controlled scanning, and triggering and data acquisition system. As the irradiation source, a tunable optical parametric oscillator (Surelite OPO Plus, Continuum, California) was pumped by a Q-switch Nd:YAG nanosecond-pulsed laser (Surelite III, Continuum, California) at a repetition rate of 10 Hz. The tuning range is from 410 to 710 nm. The laser output was coupled into a bifurcated fiber-bundle light guide with a core diameter of 185 μm (900 fibers, CeramOptec Industries, Germany). An acrylic probe was designed to position the bifurcations of the light guide around a 25-MHz single-element-focused ultrasound transducer (V324-SM, Olympus Panametrics-NDT, Massachusetts). The transducer was placed such that the focus of the transducer and the center of the illumination spot ($\sim 1\ cm^2$) were aligned. The illumination fluence was measured to be about 10 mJ/cm^2. This probe was mounted on a three-axis motion system for B-scan and C-scan imaging. A peripheral component interconnect (PCI) motion card (NI7350, National Instruments Inc., Texas) was used to control a high-precision three-axis motion stage with three integrated stepper motors (23Y002D-LW8, Anaheim Automation, California). Fast scanning was accomplished with a voice-coil actuator as previously described[25,26] while vertical and elevational translation were accomplished using the stepper motors.

Signals from the transducer were amplified by a variable-gain preamplifier then further amplified by an ultrasound pulser/receiver (5073PR, Panametrics-NDT, Massachusetts). The variable-gain stage (AD603ARZ evaluation board, Analog Devices, Massachusetts) was used to implement time-gain compensation (TGC). The TGC curves in a range of 40 dB for both ultrasound and photoacoustic imaging were controlled via a digital input–output (DIO) card (NI PCI-6542, National Instruments Inc., Texas). Signals were digitized using a multichannel data acquisition card (CS8289 Gage Cobra, Gage Applied Systems Inc., Illinois) with 12-bit dynamic range and sampling rates as high as 125 MSamples/s and postprocessed using MATLAB® (R2012a, MathWorks, Massachusetts).

Our system provided combined photoacoustic and Doppler ultrasound mode. The details are referred in our previous work.[26] In brief, a pulse sequence was generated by the DIO card and sent to interleave laser and ultrasound triggers. Photoacoustic and Doppler ultrasound images were coregistered after signal processing. A schematic of the constructed system is shown in Fig. 1, which also shows a photograph of the probe with bifurcated fiber-bundle light delivery.

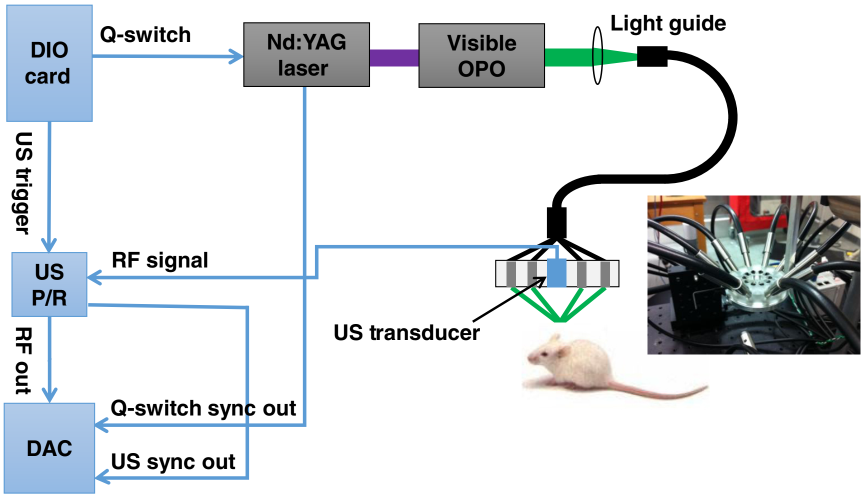

Fig. 1 A schematic of light delivery and data acquisition setup and photograph of the fiber bundle delivery surrounding the transducer. DIO, digital input–output; US, ultrasound; P/R, pulser/receiver; and DAC, data acquisition card.

2.2 *Animal Preparations*

Sprague Dawley rats (Charles River Breeding Laboratories, Massachusetts), female, weighing about 50 g, were employed in this study. Each rat was first anesthetized in an induction chamber with 1.25% to 1.5% (volume to volume) vaporized isoflurane (IsoFlo, Zoetis Inc., New Jersey). After the rat was anesthetized, it was immobilized on a customized animal holder and fitted with a nose breather. The inhaled gas was controlled by an animal anesthesia system (EZ-SA800 Single Animal System, E-Z Anesthesia, Philadelphia) mixing 1% vaporized isoflurane with certain ratios of oxygen and nitrogen. Body temperature was maintained at 37°C with a temperature—controlled heating pad, and the blood oxygenation levels and heart rates were monitored by a pulse oximeter (Nonin 8600V, Nonin Medical Inc., Minnesota) clamping on the hind leg of the animal. All *in vivo* procedures and protocols were reviewed and approved by the University of Alberta Animal Care and Use Committees.

The physiological conditions (hyperoxia, normoxia, and hypoxia) of the animal can be achieved by varying the fraction of inspired oxygen (FiO_2), which alters the arterial oxygen saturation acutely.[12] In this study, mild hypoxia and mild hyperoxia (PaO_2 within the range of 30 to 100 mm Hg) were introduced to avoid significant changes in cerebral oxygen consumption. According to Kelman's oxygen hemoglobin dissociation curve,[27] the arterial oxygen saturation should be within the range of 60% to 100%. The animal was exposed to different FiO_2 during gas anesthesia by mixing the output of regulated oxygen and nitrogen tanks with precise flow measurements read from the respective flow meters on the tanks. The global arterial oxygen saturation was recorded at each FiO_2.

2.3 *Blood Flow Estimation using Doppler Ultrasound*

Phantom imaging studies of flow estimation using double-dye mixtures and sheep blood were previously reported.[25] Pulsed color Doppler ultrasound was used for flow velocity estimation. A sequence of modulated ultrasound pulses was transmitted along a certain Doppler angle, and the flow velocities were calculated from detected phase shifts in received echoes.[28] However, when the Doppler angle approaches 90 deg, the phase shift almost vanishes and the transverse flow velocity cannot be identified. In phantom studies,[25] the appropriate Doppler angle was possible owing to oblique vessel orientation; however, the *in vivo* measurements were to be done along vessels almost perpendicular to the ultrasound beam axis. Considering the difficulty of creating such a Doppler angle with our wide-footprint probe, we adopted a different approach termed Doppler bandwidth broadening to transverse flow estimation, similar to that used in previous ultrasound and OR-PAM techniques.[23,29] In brief, assuming negligible velocity variation within the sample volume and sufficient velocity resolution, the bandwidth of the Doppler spectral broadening is given as

$$B_w = \frac{2f_0}{c_0}\frac{D}{F} v \sin\theta, \tag{2}$$

where B_w is the Doppler bandwidth, f_0 is the center frequency, c_0 is the speed of sound, D is the transducer aperture, F is the focal length, v is the flow velocity, and θ is the Doppler angle of the flow relative to the ultrasound beam axis. Since the square of Doppler bandwidth B_w can be approximated by the variance of the Doppler spectrum,[29] the transverse flow ($\theta = 90$ deg) can be estimated as

$$v_T = \frac{c_0}{2f_0}\frac{F}{D}\sqrt{\sigma^2}, \tag{3}$$

where σ^2 is the variance of Doppler spectrum, which is calculated routinely in correlation-based color Doppler ultrasound algorithm.[28]

Our system also provided power Doppler ultrasound to image blood volume fractions. Different from flow velocity estimation, the intensity of power Doppler image is proportional to the number of scatterers moving within a vascular volume rather than the frequency shifts they generate,[30] which makes it more sensitive to blood flow detection and independent of Doppler angles.[31] Since tissues surrounding blood vessels often generate much stronger scattered signals than moving blood, clutter filtering is necessary before velocity estimation and power calculations. Here, an adaptive eigenfilter was designed and implemented based on the statistics of the clutter and tissue movement. The correlation matrix of the received signals was decomposed into eigenvectors and eigenvalues by the discrete Karhunen–Loeve transform (DKLT), and then eigenvalues were sorted in decreasing amplitude. Since the eigenvalue spectrum represents the power distribution of the frequency components[32] and the power of clutter signals arising from tissues is much higher than other components, the clutter space and flow space can be partitioned in the spectrum. Appropriate filter order was determined experimentally to give the best trade-off between clutter rejection and preservation of flow.

2.4 *Oxygen Saturation Estimation Using Photoacoustic Methods*

Blood oxygen saturation (sO_2) estimation was validated in phantom studies[25] by relating photoacoustic estimates of sO_2 to sO_2 levels measured from knowledge of measured pO_2 and pH and given known oxygen dissociation curves. As this is significantly more challenging *in vivo*, in this paper, we chose to implement two independent photoacoustic methods to cross-validate sO_2 estimates. The first and most traditional approach was to solve for unknown concentration of oxy-hemoglobin $[C_{\mathrm{HbO_2}}(x)]$ and concentration of deoxy-hemoglobin $[C_{\mathrm{Hb}}(x)]$, given measured photoacoustic signals $p(x,\lambda_k)$ and known molar extinction coefficients $\varepsilon_{\mathrm{Hb}}(\lambda_k)$ and $\varepsilon_{\mathrm{HbO_2}}(\lambda_k)$

$$\begin{bmatrix} p(x,\lambda_1) \\ \vdots \\ p(x,\lambda_n) \end{bmatrix} = \Gamma(x) \begin{bmatrix} \Phi(x,\lambda_1)\varepsilon_{\mathrm{Hb}}(\lambda_1) & \Phi(x,\lambda_1)\varepsilon_{\mathrm{HbO_2}}(\lambda_1) \\ \vdots & \vdots \\ \Phi(x,\lambda_n)\varepsilon_{\mathrm{Hb}}(\lambda_n) & \Phi(x,\lambda_n)\varepsilon_{\mathrm{HbO_2}}(\lambda_n) \end{bmatrix} \begin{bmatrix} C_{\mathrm{Hb}}(x) \\ C_{\mathrm{HbO_2}}(x) \end{bmatrix}. \tag{4}$$

This approach suffers from unknown wavelength-dependent fluence $\Phi(x,\lambda_k)$, which is often assumed a constant or requires wavelength-dependent calibration. The relative Gruneisen parameter and relative sensitivity are lumped into the wavelength-independent factor $\Gamma(x)$ and will not impact the estimate of oxygen saturation of hemoglobin

$$sO_2(x) = \frac{C_{HbO_2}(x)}{C_{Hb}(x) + C_{HbO_2}(x)} \times 100\%. \tag{5}$$

A second approach, proposed in Ref. 33, is to use multiwavelength photoacoustic measurements at different oxygen saturation levels and solve a system of equations to estimate the different sO_2 levels. The absorption coefficients given two sO_2 levels can be written as

$$\mu_{a1}(x, \lambda i) = \{\varepsilon_{Hb}(\lambda i)[1 - sO_2^{(1)}(x)] + \varepsilon_{HbO_2}(\lambda i) sO_2^{(1)}(x)\} C_{HbT}(x), \tag{6}$$

$$\mu_{a2}(x, \lambda i) = \{\varepsilon_{Hb}(\lambda i)[1 - sO_2^{(2)}(x)] + \varepsilon_{HbO_2}(\lambda i) sO_2^{(2)}(x)\} C_{HbT}(x), \tag{7}$$

where $C_{HbT}(x)$ is the total concentration of hemoglobin. The sO_2 at the respective time points can thus be estimated from photoacoustic measurements as

$$sO_2^{(1)} = \frac{b p_2(\lambda_1) - a p_2(\lambda_2)}{p_1(\lambda_2) p_2(\lambda_1) - p_1(\lambda_1) p_2(\lambda_2)}, \tag{8}$$

$$sO_2^{(2)} = \frac{b p_1(\lambda_2) - a p_1(\lambda_1)}{p_1(\lambda_2) p_2(\lambda_1) - p_1(\lambda_1) p_2(\lambda_2)}, \tag{9}$$

with

$$a = \frac{[p_1(\lambda_1) - p_2(\lambda_1)]\varepsilon_{Hb}(\lambda_1)}{\varepsilon_{HbO_2}(\lambda_1) - \varepsilon_{Hb}(\lambda_1)}, \tag{10}$$

$$b = \frac{[p_1(\lambda_2) - p_2(\lambda_2)]\varepsilon_{Hb}(\lambda_2)}{\varepsilon_{HbO_2}(\lambda_2) - \varepsilon_{Hb}(\lambda_2)}. \tag{11}$$

This approach requires no wavelength-dependent fluence calibration factor but assumes that the optical properties of tissue between the vessels of investigation and the tissue surface do not change their optical properties. Thus, neither approach is devoid of approximations, yet consistency in estimates would provide cross substantiation.

2.5 *Cerebral Metabolic Rate of Oxygen Consumption Estimation*

According to Eq. (1), assuming that CBF is the only way of oxygen delivery to the brain, the global $CMRO_2$ can be estimated by combining the measurements of CBF, arterial oxygen saturation ($sO_{2,a}$), and venous oxygen saturation ($sO_{2,v}$)

$$CMRO_2 = CBF \times C_{HbT} \times \tau \times (sO_{2,a} - sO_{2,v}), \tag{12}$$

where C_{HbT} is the total concentration of hemoglobin with a unit of g/ml and τ is the oxygen-carrying capacity of 1.39-ml oxygen per gram of hemoglobin on the basis of a typical C_{HbT} level (0.147 g/ml at a hematocrit of 0.42).[34] Based on anatomic and hemodynamic studies,[1,2] oxygen is supplied to the brain by four feeding vessels: the left and right internal carotid arteries and the left and right vertebral arteries. Although the contribution of each artery to the total cerebral perfusion is different, the oxygen saturation levels in these vessels are comparable to each other. For the blood draining from the brain, the pair of internal jugular veins provides the majority (~80%) of the venous drainage via deep veins and dual sinuses. In our *in vivo* study, the combined imaging system scanned across the neck of the subject and the $sO_{2,a}$ and $sO_{2,v}$ were estimated from the carotid artery and jugular vein in the field of view. For CBF estimation, we used flow rates of internal jugular veins by measuring the cross-sectional area ($\overline{A}_{IJV}$) and the mean flow velocity ($\overline{v}_{IJV}$) of the vessel. Thus, the representative $CMRO_2$ can be expressed as

$$CMRO_2 = \overline{A}_{IJV} \times \overline{v}_{IJV} \times C_{HbT} \times \tau \times (sO_{2,a} - sO_{2,v}). \tag{13}$$

The unit for $CMRO_2$ is ml/100 g/ min of the tissue.

3 Results

First, the bandwidth broadening Doppler ultrasound approach was validated in phantoms with embedded tubing by comparing estimated flow velocity against preset flow speeds, as shown in Fig. 2. The construction of the cornstarch-gelatin phantom can be referred to our previous work.[31] Under the assumption of fully developed parabolic flow, we observed excellent consistency and sensitivity to flow velocities of several mm/s, sufficient for *in vivo* flow estimation in murine carotid artery and jugular veins. The correlation of determination R^2 of linear least-square fitting is 0.99 with a slope of 0.94 and a zero-offset of 4.2 mm/s.

Next, we estimated $CMRO_2$ *in vivo* using Doppler ultrasound for flow estimation and multiwavelength photoacoustic methods for sO_2 estimation. The animal was prepared as described in Sec. 2.2 and scanned across the neck at the speed of 5 mm/s under different physiological conditions. The global arterial sO_2 was recorded by the pulse oximeter during the modulation of FiO_2. Figure 3 shows representative *in vivo* coregistered photoacoustic (acquired at 580 nm), Doppler bandwidth broadening, and power Doppler images of the carotid artery and jugular vein when global arterial sO_2 was measured at 85%. The artery was located >2 mm in depth, and the vein was located ~1 mm under the skin. As in Fig. 3(b), the

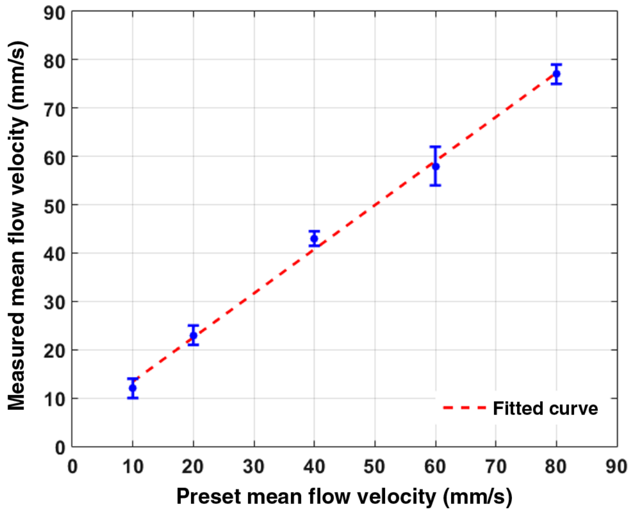

Fig. 2 Comparison between the preset and the measured flow velocity of phantom using Doppler bandwidth broadening

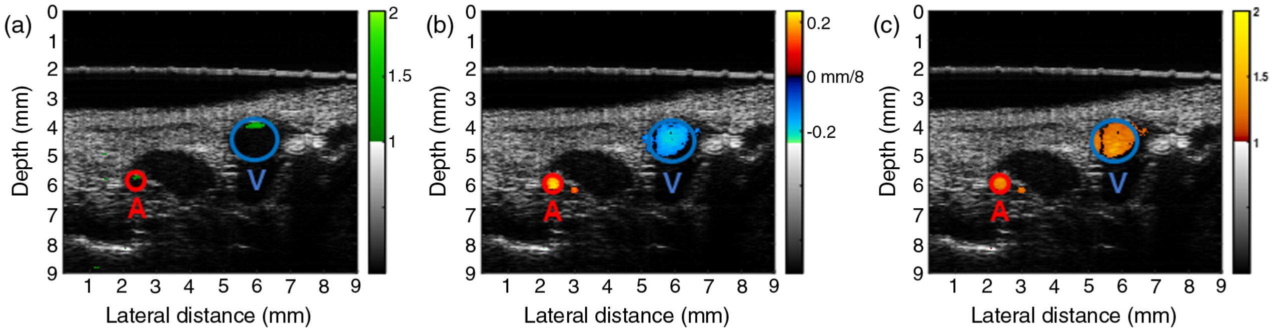

Fig. 3 Representative *in vivo* coregistered images of carotid artery (labeled as "A") and jugular vein (labeled as "V"): (a) photoacoustic image acquired at 580 nm, (b) Doppler bandwidth broadening image, the color bar shows the absolute value of flow speed and direction, and (c) power Doppler image.

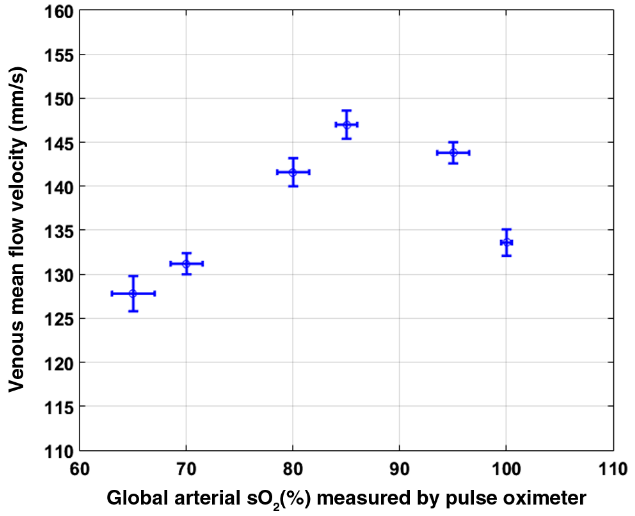

Fig. 4 Venous mean flow velocities measured from hyperoxia (global arterial sO_2 ~100%) to hypoxia (global arterial sO_2 ~65%) conditions.

mean flow speed was quantified as 146 mm/s. For the task of cross-sectional area estimation, a circular region was selected so that all the color pixels in the power Doppler image [Fig. 3(c)] were fitted into the circle.

Figure 4 shows the measured venous mean flow velocities as a function of global arterial sO_2 measured by the pulse oximeter. The appropriate ultrasound pulse-repetition-rate was chosen to ensure that the flow speeds were within the detectable range.[35] The mean flow velocity of the internal jugular vein begins to drop above a global arterial sO_2 of $\tilde{8}5\%$.

Figure 5 shows photoacoustic sO_2 estimates in both arteries and veins as a function of measured global arterial sO_2 from a pulse oximeter. As described in Sec. 2.4, we used two photoacoustic methods to cross validate our sO_2 estimation. Method 1 is the traditional approach, which solves for unknown concentrations of oxy- and deoxy-hemoglobin using measured photoacoustic signals and known molar extinction coefficients, whereas method 2 uses multiwavelength photoacoustic measurements at different sO_2 levels to solve a system of equations to estimate the different sO_2 levels. Figure 5(a) shows the comparison of arterial sO_2 estimations between method 1 and

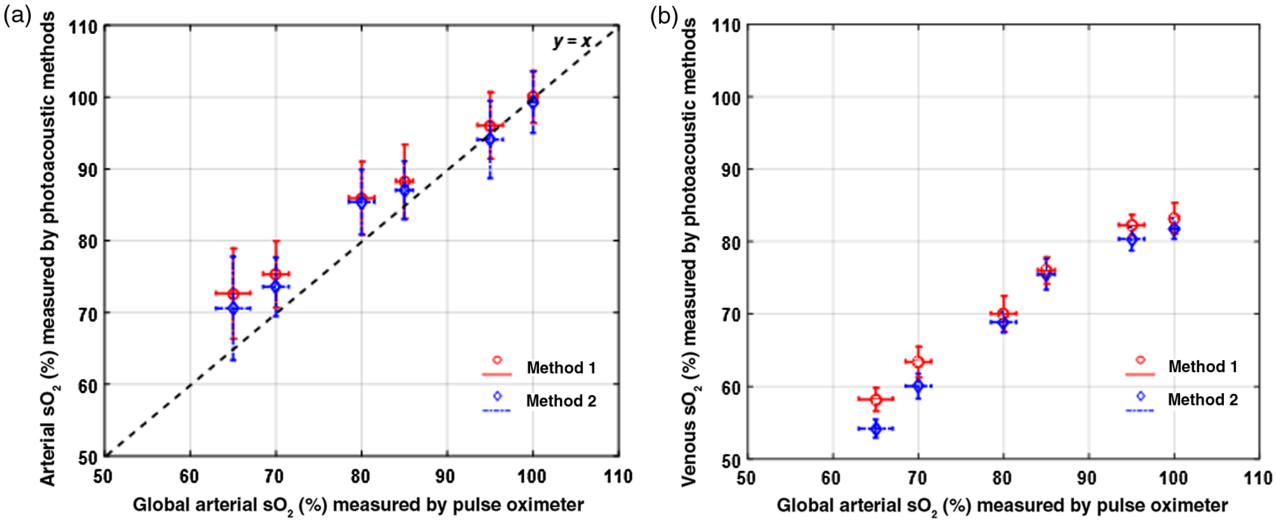

Fig. 5 Comparison of photoacoustic sO_2 estimations between method 1 and method 2 in (a) carotid artery and (b) jugular vein. The arterial sO_2 error bars are larger than venous sO_2 error bars, likely due to flow pulsatility in arteries.

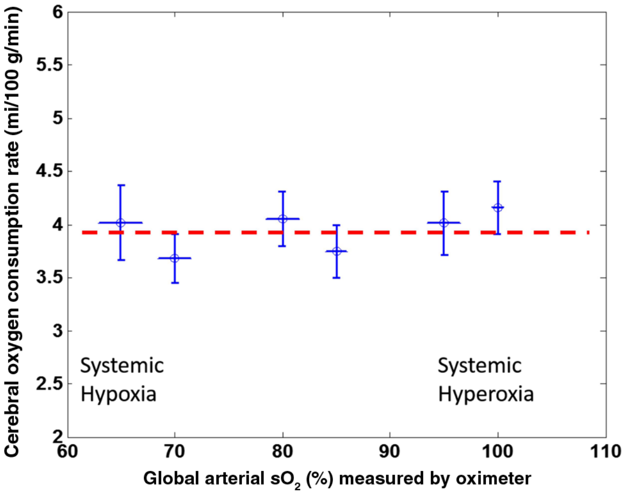

Fig. 6 The estimated representative CMRO_2 (ml/100 g/min) as a function of varying global arterial sO_2 measured using pulse oximetry during modulation of FiO_2 under anesthesia. Error bars are standard deviations estimated according to the theory of propagation of errors.

method 2. The estimates are consistent with $p < 0.05$. It can also be observed that the sO_2 estimates from arteries are close to the pulse oximeter values. The consistency ensures the validation of sO_2 estimation in arteries and offers confidence in sO_2 estimation in veins.

The representative CMRO_2 was quantified according to Eq. (9) in Sec. 2.5. Here, we used a typical C_{HbT} level of 0.147 g/ml at a hematocrit of 0.42.[34] The results are shown in Fig. 6 as a function of global arterial sO_2 as measured using pulse oximetry. As anticipated, the CMRO_2 remains relatively constant during mild hypoxia and hyperoxia (global arterial sO_2 of 65% to 100%), consistent with the hypothesis of brain metabolic autoregulation.

4 Discussion

Given the major significance of oxygen metabolism in health and disease, our work represents an approach to measure this metric using photoacoustic and ultrasound technologies. Current efforts use high-frequency ultrasound and visible light for animal models owing to limited penetration requirements. It should be noted, however, that depths investigated represent unreachable penetrations for previous oxygen metabolism progress using OR-PAM.

In this study, the total CBF is quantified by measuring outflow instead of inflow,[36] as internal jugular veins provide the majority (~80%) of the venous drainage from the brain. Since not all the blood vessels are counted for the measurements, the CMRO_2 we measure is only a representative measure of oxygen consumption. Given the bifurcation of the common carotid artery into internal and external, our estimate of CMRO_2 may be influenced by including facial oxygen flux. Encouragingly, the representative CMRO_2 remains relatively constant during the modulation of the FiO_2, which agrees with the hypothesis of cerebral metabolic autoregulation in the range of 23 to 100 mm Hg of PaO_2. During mild hypoxia, the metabolic demand may be met by elevated CBF or higher extraction of oxygen from the blood.[11] We have observed that the mean flow speed of internal jugular vein was dropping at global arterial sO_2 of ~85%. This may be the consequence of vasodilation, which helps to increase the cerebral blood volume under the hypoxia condition.[2]

Uncertainty due to measurement variability is quantified by measuring sO_2 and flow rates at least three times and estimating standard deviations. Future work should aim to reduce uncertainties by optimization of light fluence, using higher-sensitivity detectors, and by a potential combination of motion compensation and judicious averaging. Array transducers may improve frame rates to real time if sufficient wavelength-switching capabilities are available, whereas current ultrasound B-scan speeds are limited to ~15 fps while photoacoustic B-scans are limited by the 10-Hz repetition rate of the laser to acquire a single A-scan.

Future work should investigate conditions where brain autoregulation is impacted, such as stroke, trauma, acute sepsis, brain damage, and potentially neurodegenerative conditions. Preclinical investigation with animal models may offer invaluable insight prior to human translation. Human translation may be possible with infrared light and diagnostic-frequency transducers, especially in infants and children, considering the superficial depths of internal carotid and jugular vessels in these subjects.

5 Conclusion

We have demonstrated *in vivo* estimation of CMRO_2 metabolism in murine models using a custom combined photoacoustic and microultrasound system. Estimates of CMRO_2 are based on arterial and venous oxygen saturation measurements using photoacoustic methods and flow measurements based on Doppler ultrasound. Photoacoustic estimates of oxygen saturation in arteries are validated with pulse oximetry while venous sO_2 is cross validated using two independent photoacoustic methods. The estimated CMRO_2 remains relatively constant from mild hypoxia to mild hyperoxia conditions, which agrees with the hypothesis of cerebral metabolic autoregulation. The demonstrated method for estimating oxygen consumption may have significant applicability in other tissues and has potential for clinical translation owing to its label free nature.

Disclosures

Roger Zemp is the cofounder and chief scientific officer of illumiSonics Inc., which, however, did not support this work. The authors have no other disclosures or conflicts of interest to report.

Acknowledgments

We gratefully acknowledge funding from the Canadian Institutes of Health Research (No.CPG 134739), the Natural Sciences and Engineering Research Council of Canada (Nos. NSERC 355544-2008, 375340-2009, STPGP 396444, EQPEQ 440290, EQPEQ 423474, EQPEQ 423197, RGPIN 355544, and STPGP 494293-16), the Canadian Cancer Society (Nos. CCS 2011-700718 and CCS 702032), and the Prostate Cancer Canada (No. PCC MVBRDG D2013-40).

References

1. R. J. Person and R. Thies, *Physiology*, 2nd ed., Springer-Verlag Inc., New York (1989).
2. R. C. Tasker, "Brain vascular and hydrodynamic physiology," *Semin. Pediatr. Surg.* **23**(4), 168–173 (2013).
3. K. Ishii et al., "Decreased medical temporal oxygen metabolism in Alzheimer's disease shown by PET," *J. Nucl. Med.* **37**(7), 1159–1165 (1996).

4. R. F. Peppard et al., "Cerebral glucose metabolism in Parkinson's disease with and without dementia," *Arch. Neurol.* **49**(12), 1262–1268 (1992).
5. P. Santens et al., "Cerebral oxygen metabolism in patients with progressive supranuclear palsy: a positron emission tomography study," *Eur. Neurol.* **37**, 18–22 (1997).
6. V. Bonhomme et al., "Influence of anesthesia on cerebral blood flow, cerebral metabolic rate, and brain functional connectivity," *Curr. Opin. Anesthesiol.* **24**(5), 474–479 (2011).
7. A. A. Scand, "Regional cerebral blood flow and glucose metabolism during propofol anesthesia in healthy subjects studied with positron emission tomography," *Acta Anaesthesiol. Scand.* **56**(2), 248–255 (2012).
8. J. B. De Vis et al., "Calibrated MRI to evaluate cerebral hemodynamics in patients with an internal carotid artery occlusion," *J. Cereb. Blood Flow Metab.* **35**(6), 1015–1023 (2015).
9. M. N. Diringer et al., "Effect of hyperoxia on cerebral metabolic rate for oxygen measured using positron emission tomography in patients with acute severe head injury," *J. Neurosurg.* **106**(4), 526–529 (2007).
10. S. S. Kety and C. F. Schmidt, "The effect of altered arterial tensions of carbon dioxide and oxygen on cerebral blood flow and cerebral oxygen consumption of normal young men," *J. Clin. Invest.* **27**(4), 484–492 (1948).
11. S. P. Chong et al., "Cerebral metabolic rate of oxygen ($CMRO_2$) assessed by combined Doppler and spectroscopic OCT," *Biomed. Opt. Express* **6**(10), 3941–3951 (2015).
12. F. Xu et al., "Effect of hypoxia and hyperoxia on cerebral blood flow, blood oxygenation, and oxidative metabolism," *J. Cereb. Blood Flow Metab.* **32**(10), 1909–1918 (2012).
13. M. J. Cipolla, *The Cerebral Circulation*, Morgan and Claypool Life Sciences, San Rafael, California (2009).
14. T. Christen, D. S. Bolar, and G. Zaharchuk, "Imaging brain oxygenation with MRI using oxygenation approaches: methods, validation, and clinical applications," *Am. J. Neuroradiol.* **34**(6), 1113–1123 (2013).
15. T. S. Mayberg and A. M. Lam, "Jugular bulb oximetry for the monitoring of cerebral blood flow and metabolism," *Neurosurg. Clin. N. Am.* **7**(4), 755–765 (1996).
16. Y. Yamamoto et al., "Noninvasive quantification of regional myocardial metabolic rate of oxygen by $^{15}O_2$ inhalation and positron emission tomography," *Circulation* **94**, 808–816 (1996).
17. E. M. Haacke et al., "In vivo measurement of blood oxygen saturation using magnetic resonance imaging: a direct validation of the blood oxygen level-dependent concept in functional brain imaging," *Hum. Brain Mapp.* **5**, 341–346 (1997).
18. V. Jain, M. C. Langham, and F. W. Wehrli, "MRI estimation of global brain oxygen consumption rate," *J. Cereb. Blood Flow Metab.* **30**(9), 1598–1607 (2010).
19. G. Yu et al., "Time-dependent blood flow and oxygenation in human skeletal muscles measured with noninvasive near-infrared diffuse optical spectroscopies," *J. Biomed. Opt.* **10**(2), 024027 (2005).
20. L. A. Steiner et al., "Near-infrared spectroscopy can monitor dynamic cerebral autoregulation in adults," *Neurocrit. Care* **10**(1), 122–128 (2009).
21. L. V. Wang, "Prospects of photoacoustic tomography," *Med. Phys.* **35**(12), 5758–5767 (2008).
22. J. Yao et al., "Label-free oxygen-metabolic photoacoustic microscopy in vivo," *J. Biomed. Opt.* **16**(7), 076003 (2011).
23. J. Yao and L. V. Wang, "Transverse flow imaging based on photoacoustic Doppler bandwidth broadening," *J. Biomed. Opt.* **15**(2), 021304 (2010).
24. J. Brunker and P. Beard, "Velocity measurements in whole blood using acoustic resolution photoacoustic Doppler," *Biomed. Opt. Express* **7**(7), 2789–2806 (2016).
25. Y. Jiang et al., "Blood oxygen flux estimation with a combined photoacoustic and high-frequency ultrasound microscopy system: a phantom study," *J. Biomed. Opt.* **17**(3), 036012 (2012).
26. T. Harrison et al., "Combined photoacoustic and ultrasound biomicroscopy," *Opt. Express* **17**, 22041–22046 (2009).
27. G. R. Kelman, "Digital computer subroutine of the conversion of oxygen tension into saturation," *J. Appl. Physiol.* **21**(4), 1375–1376 (1966).
28. C. Kasai et al., "Real-time two-dimensional blood flow imaging using an autocorrelation technique," *IEEE Trans. Sonics Ultrason.* **32**, 458–464 (1985).
29. B. Lee et al., "Doppler angle and flow velocity estimations using the classic and transverse Doppler effects," *IEEE Trans. Ultrason. Ferroelectr. Freq. Control* **46**(1), 252–256 (1999).
30. J. M. Rubin et al., "Power Doppler US: a potentially useful alternative to mean frequency-based color Doppler US," *Radiology* **190**, 853–856 (1994).
31. Y. Jiang et al., "Photoacoustic and high-frequency power Doppler ultrasound biomicroscopy: a comparative study," *J. Biomed. Opt.* **15**(5), 056008 (2010).
32. D. E. Kruse and K. W. Ferrara, "A new high resolution color flow system using an eigendecomposition-based adaptive filter for clutter rejection," *IEEE Trans. Ultrason. Ferroelectr. Freq. Control* **49**(12), 1739–1754 (2002).
33. J. Xia et al., "Calibration-free quantification of absolute oxygen saturation based on the dynamics of photoacoustic signals," *Opt. Lett.* **38**(15), 2800–2803 (2013).
34. J. B. West, *Pulmonary Physiology and Pathophysiology: An Integrated, Case-Based Approach*, 2nd ed., Lippincott Williams & Wilkins, Philadelphia (2007).
35. R. S. C. Cobbold, *Foundations of Biomedical Ultrasound*, Oxford University Press, New York (2007).
36. H. Ohsumi et al., "Internal jugular bulb blood velocity as a continuous indicator of cerebral blood flow during open heart surgery," *Anesthesiology* **81**(2), 325–332 (1994).

Biographies for the authors are not available.